Recovery of optical cross-section perturbations in dense-scattering media by transport-theory-based imaging operators and steady-state simulated data

Jenghwa Chang, Harry L. Graber, Randall L. Barbour, and Raphael Aronson

We present a useful strategy for imaging perturbations of the macroscopic absorption cross section of dense-scattering media using steady-state light sources. A perturbation model based on transport theory is derived, and the inverse problem is simplified to a system of linear equations, $\mathbf{W}\Delta\boldsymbol{\mu} = \Delta\mathbf{R}$, where $\mathbf{W}$ is the weight matrix, $\Delta\boldsymbol{\mu}$ is a vector of the unknown perturbations, and $\Delta\mathbf{R}$ is the vector of detector readings. Monte Carlo simulations compute the photon flux across the surfaces of phantoms containing simple or complex inhomogeneities. Calculation of the weight matrix is also based on the results of Monte Carlo simulations. Three reconstruction algorithms—conjugate gradient descent, projection onto convex sets, and the simultaneous algebraic reconstruction technique, with or without imposed positivity constraints—are used for image reconstruction. A rescaling technique that improves the conditioning of the weight matrix is also developed. Results show that the analysis of time-independent data by a perturbation model is capable of resolving the internal structure of a dense-scattering medium. Imposition of positivity constraints improves image quality at the cost of a reduced convergence rate. Use of the rescaling technique increases the initial rate of convergence, resulting in accurate images in a smaller number of iterations.

Key words: Dense-scattering medium, inverse problem, perturbation, ill posed.

1. Introduction

Many clinical imaging modalities that have been developed during the past two to three decades—e.g., x-ray computed tomography (CT), positron-emission tomography (PET), single-photon-emission computed tomography (SPECT), and magnetic resonance imaging (MRI)—employ forms of energy whose propagation through biological tissues are weak-scattering processes.[1,2] Consequently, simple two-dimensional (2-D) projection imaging can produce interpretable images even of thick structures. Moreover, tomographic imaging techniques based on the Radon transform and filtered backprojection algorithms based on the Fourier slice theorem[3–5] or Fourier diffraction theory[4,5] can produce detailed, high-resolution anatomical maps of 2-D sections of a person or another target medium. The spatial resolution presently achievable in x-ray CT imaging is >200 pixels/cm^2 within a 1-mm-thick slice.[6] A much more difficult problem is imaging based on analysis of measurements of highly scattered signals, such as red and near-infrared electromagnetic radiation (i.e., approximately 0.7–1.3-μm wavelengths) propagating through biological tissues, which are weakly absorbing in this range. "Photon-migration imaging" and "optical diffusion tomography" (ODT) have been suggested as names for the proposed imaging technique; image reconstruction in this case amounts to solving the three-dimensional (3-D) inverse scattering problem, and the methods successfully employed in the low-scattering imaging modalities are inapplicable.

The diagnostic potential of ODT is sufficiently

J. Chang, H. L. Graber, and R. L. Barbour are with the State University of New York Health Science Center at Brooklyn, Brooklyn, N.Y. 11203; J. Chang is with the Department of Pathology, H. L. Graber is with the Department of Physiology and Biophysics, and R. L. Barbour is with the Department of Pathology and the Department of Physiology and Biophysics. R. Aronson is with Bioimaging Sciences Corporation, West Orange, New Jersey, 07052.

Received 24 April 1995; revised manuscript received 8 December 1995.

0003-6935/96/203963-16$10.00/0

great that many groups of researchers in several countries are now actively engaged in basic research in this area.[7–9] As an example of this potential, hemoglobin and other heme-bearing proteins are among the endogenous compounds largely responsible for the absorption that does occur at red and near-infrared wavelengths. Reconstructed images of the absorption cross section can be related to the spatially varying concentrations of the different chemical or electronic states of these compounds,[10] and physiological and functional information not provided by other imaging modalities can be inferred from these relations. Imaging the scattering cross section should also be possible and could have diagnostic value in itself, as scattering appears to occur principally at the boundaries of intracellular organelles,[11] and in an incipient disease state, scattering changes may well precede anatomical changes detectable by other imaging techniques. In addition, it should be possible with ODT to image the spatial distributions of exogenous tracers, which may be detected by their effect on either absorption or on scattering, or by fluorescence. Further, ODT techniques may be generalizable to other, nonbiological, imaging problems, thereby increasing their range and the size and the complexity of the targets that can be studied. There could well be, for example, geologic, oceanographic, and astrophysical applications.

Because the target medium in an ODT measurement is both heterogeneous and strongly scattering, filtered backprojection and transform-based reconstruction algorithms are inapplicable. However, an alternative, algebraic, mathematical framework in which to approach the image-reconstruction problem is available. If the unknown distribution of target properties can be recast as a small perturbation from a known reference state, then the tomographic imaging problem is expressible mathematically as a system of linear equations; recovery of the image is equivalent to solving the linear system.[3–5] As we discuss below, experience shows that this approach works even when the perturbation is not especially small. Algorithms that have been successfully used in diagnostic imaging include direct matrix inversion (Gaussian elimination, or LU decomposition), singular-value decomposition, and iterative methods. Direct matrix inversion and singular-value decomposition are very efficient for small problems, i.e., below a threshold size, but are generally not suitable for inversion of large matrices, and they are rarely used in practical image reconstructions. The iterative methods, which repeatedly update the reconstructed images according to the detected signals and *a priori* information, are particularly suitable for large-scale inverse problems; moreover, unlike the direct-matrix-inversion and the singular-value-decomposition methods, useful images may be obtained even after a small number of iterations.

In earlier published reports,[12–19] we have presented reconstructed images of both simulated targets and laboratory phantoms consisting of a small number (1–3) of absorbing heterogeneities embedded in a strongly scattering, homogeneous background medium. These image reconstructions employed several algorithms, differing sets of detectors [e.g., detectors surrounding the target in some cases but only on the same surface as the source (i.e., backscattering) in others], different combinations of constraints and regularization techniques, and different source types (steady-state measurements in some cases and time-resolved measurements in others). In the present study we extended these analyses and compare three reconstruction algorithms: projection onto convex sets[20] (POCS), conjugate-gradient descent[21,22] (CGD), and the simultaneous iterative reconstruction technique[4,23] (SART). Image quality and convergence rates were evaluated for both 2-D and 3-D versions of each algorithm. Also presented are results of an examination of the effects produced by several elementary regularization methods[24] and of the dependence of image quality on the number of sources as well as on the location and the orientation of the sources with respect to the target surface.

2. Perturbation Model

It is generally accepted that for the sorts of problems addressed in this report, photons may be treated as if they were classical particles and that in such a regime the migration of monoenergetic photons from a steady-state, or continuous-wave (cw), source through an isotropic medium can be described by the time-independent one-speed transport equation[25,26]:

$$\mathbf{\Omega}\cdot\nabla\phi(\mathbf{r},\mathbf{\Omega})+\mu_T(\mathbf{r})\phi(\mathbf{r},\mathbf{\Omega})-\int_{4\pi}\mu_s(\mathbf{r},\mathbf{\Omega}'\cdot\mathbf{\Omega})\times\phi(\mathbf{r},\mathbf{\Omega}')\mathrm{d}\Omega'=s(\mathbf{r},\mathbf{\Omega}),\quad(1)$$

where $\mathrm{d}\Omega$ is the differential solid angle about the direction Ω of photon motion, $\mathbf{\Omega}$ is the unit vector in the direction $\mathbf{\Omega}$, $\phi(\mathbf{r},\mathbf{\Omega})$ is the angular intensity at position $\mathbf{r}$ in direction Ω (photons per unit area, unit solid angle, and unit time), $s(\mathbf{r},\mathbf{\Omega})$ is the angular source density at $\mathbf{r}$ in direction Ω (photons per unit volume, unit solid angle, and unit time), $\mu_s(\mathbf{r},\mathbf{\Omega}'\cdot\mathbf{\Omega})$ is the macroscopic differential scattering cross section at $\mathbf{r}$ from direction Ω' into direction Ω (inverse length per unit solid angle), $\mu_s(\mathbf{r})=\int_{4\pi}\mu_s(\mathbf{r},\mathbf{\Omega}\cdot\mathbf{\Omega}')\mathrm{d}\Omega'$ is the macroscopic scattering cross section (inverse length), $\mu_a(\mathbf{r})$ is the macroscopic absorption cross section (inverse length), and $\mu_T(\mathbf{r})=\mu_a(\mathbf{r})+\mu_s(\mathbf{r})$ is the macroscopic total cross section (inverse length).

We restrict further discussion to changes in absorption, but the extension to changes in scattering is immediate. We derived the perturbation model[5,27] adopted for absorption cross sections in this study by introducing perturbations of the cross sections and intensity, $\mu_a\rightarrow\mu_a+\Delta\mu_a$ and $\phi\rightarrow\phi+\Delta\phi$, into Eq. (1) and truncating the terms proportional to $\Delta\mu_a\Delta\phi$. This is our basic linearity assumption. It holds for sufficiently small $\Delta\mu_a$.

The general expression for the corresponding change, ΔR, in the detector response in the linear regime is

$$\Delta R = \int_V w_a(\mathbf{r})\Delta\mu_a(\mathbf{r})\mathrm{d}^3r, \tag{2}$$

where $w_a(\mathbf{r})$ is the appropriate weight function at $\mathbf{r}$.

The adjoint angular intensity, $\phi^+(\mathbf{r}, \mathbf{\Omega})$, is defined as the detector response that is due to one photon born per second at $\mathbf{r}$ and emitted in direction Ω. The change in absorption density at $\mathbf{r}$ in $\mathrm{d}\Omega$ that is due to $\Delta\mu_a$ is $\Delta\mu_a(\mathbf{r})\phi(\mathbf{r}, \mathbf{\Omega})\mathrm{d}\Omega$. The corresponding change in the total detector response is then

$$\Delta R = -\int_V\int_{4\pi} \Delta\mu_a(\mathbf{r})\phi(\mathbf{r}, \mathbf{\Omega})\phi^+(\mathbf{r}, \mathbf{\Omega})\mathrm{d}\Omega\mathrm{d}^3r. \tag{3}$$

Our linearity assumption implies that both ϕ and ϕ^+ are to be computed for the unperturbed medium. Comparison of Eqs. (2) and (3) gives

$$w_a(\mathbf{r}) = -\int_{4\pi} \phi(\mathbf{r}, \mathbf{\Omega})\phi^+(\mathbf{r}, \mathbf{\Omega})\mathrm{d}\Omega. \tag{4}$$

If we can reasonably neglect the angular correlations between ϕ and ϕ^+, for instance, if either one is nearly isotropic, then Eq. (4) reduces to

$$w_a(\mathbf{r}) = \frac{-1}{4\pi}\,\phi(\mathbf{r})\phi^+(\mathbf{r}), \tag{5}$$

where $\phi(\mathbf{r})$ and $\phi^+(\mathbf{r})$ are, respectively, the total direct intensity and adjoint intensities:

$$\phi(\mathbf{r}) = \int_{4\pi} \phi(\mathbf{r}, \mathbf{\Omega})\mathrm{d}\Omega,$$

$$\phi^+(\mathbf{r}) = \int_{4\pi} \phi^+(\mathbf{r}, \mathbf{\Omega})\mathrm{d}\Omega.$$

As for the assumption that the angular correlation between ϕ and ϕ^+ is negligible, if $\phi(\mathbf{r}, \mathbf{\Omega})$ and $\phi^+(\mathbf{r}, \mathbf{\Omega})$ are expanded in spherical harmonics, one can show that the lowest-order correction term to w_a is $3\mathbf{J}(\mathbf{r}) \cdot \mathbf{J}^+(\mathbf{r})/4\pi$, where $\mathbf{J}$ and $\mathbf{J}^+$ are the direct and adjoint fluxes, respectively. Since $|\mathbf{J}(\mathbf{r}) \cdot \mathbf{J}^+(\mathbf{r})| \le |\mathbf{J}(\mathbf{r})|\,|\mathbf{J}^+(\mathbf{r})| \le \phi(\mathbf{r})\phi^+(\mathbf{r})$ and the inequalities are usually satisfied quite strongly, the correction is usually small compared with the term we retained in Eq. (5). [The $1/4\pi$ factor in Eq. (5) results from the normalization we chose here for ϕ^+. A different choice would give a different factor.]

Finally, $\phi^+(\mathbf{r}, \Omega)$ has a well-known alternative interpretation as the angular intensity at $(\mathbf{r}, -\mathbf{\Omega})$ that is due to a source $r(\mathbf{r}_d, -\mathbf{\Omega}_d)$, where $r(\mathbf{r}_d, \mathbf{\Omega}_d)$ is the detector response function for photons entering the detector at $\mathbf{r}_d$ in direction Ω_d.[28] Thus the adjoint intensity can be computed as the solution to a forward problem.

For numerical implementation of the perturbation equation, consider a medium divided into a set of J small, contiguous, nonoverlapping volume elements, or voxels. The voxel shapes are arbitrary, and they are sufficiently small that the optical properties μ_a and μ_s do not vary significantly within a voxel. Letting V_j be the volume of voxel j, $j = 1, 2, \ldots, J$, the discretized version of perturbation Eq. (2) for source–detector pair i, $i = 1, 2, \ldots, I$, is

$$\Delta R_i = \sum_j w_{a,ij}\Delta\mu_{a,j}, \tag{6}$$

where ΔR_i is the change (perturbation) in detector reading associated with source–detector pair i, $\Delta\mu_{a,j}$ is the averaged perturbation of absorption cross section in voxel j, and $w_{a,ij}$ is the integrated absorption weight function of voxel j for source–detector pair i.

The above linear perturbation equation can also be represented in matrix form:

$$\mathbf{W}_a\Delta\boldsymbol{\mu}_a = \Delta\mathbf{R}, \tag{7}$$

where

$$\mathbf{W}_a = \begin{bmatrix} w_{a,11} & w_{a,12} & \cdots & w_{a,1J} \\ w_{a,21} & w_{a,22} & \cdots & w_{a,2J} \\ \vdots & \vdots & \ddots & \vdots \\ w_{a,I1} & w_{a,I2} & \cdots & w_{a,IJ} \end{bmatrix},$$

$$\Delta\boldsymbol{\mu}_a = \begin{bmatrix} \Delta\mu_{a,1} \\ \Delta\mu_{a,2} \\ \vdots \\ \Delta\mu_{a,J} \end{bmatrix}, \quad \Delta\mathbf{R} = \begin{bmatrix} \Delta R_1 \\ \Delta R_2 \\ \vdots \\ \Delta R_I \end{bmatrix}.$$

The inverse problem can be stated: Given a set of source–detector pairs, the perturbed detector readings $\Delta\mathbf{R}$, and the precalculated weight function $\mathbf{W}_a$, find the perturbation of the macroscopic absorption coefficients $\Delta\boldsymbol{\mu}_a$ of the target medium using Eq. (7).

3. Reconstruction Algorithms

A. Iterative Methods

We obtain the least-squares solution to a system of linear equations by iteratively modifying the unknowns $\Delta\boldsymbol{\mu}_a$ to minimize the mean-squared error E:

$$\begin{aligned} E &= \tfrac{1}{2}(\mathbf{W}\Delta\boldsymbol{\mu}_a - \Delta\mathbf{R})^T(\mathbf{W}\Delta\boldsymbol{\mu}_a - \Delta\mathbf{R}) \\ &= \tfrac{1}{2}\Delta\boldsymbol{\mu}_a^T\mathbf{A}\Delta\boldsymbol{\mu}_a - \mathbf{b}^T\Delta\boldsymbol{\mu}_a + \tfrac{1}{2}\Delta\mathbf{R}^T\Delta\mathbf{R}, \end{aligned} \tag{8}$$

where $\mathbf{A} = \mathbf{W}^T\mathbf{W}$ and $\mathbf{b} = \mathbf{W}^T\Delta\mathbf{R}$. Any vector $\Delta\boldsymbol{\mu}_a$ minimizing E is a least-squares solution. We find such a solution by setting the derivative of E to 0:

$$\mathbf{g}(\Delta\boldsymbol{\mu}_a) = \frac{\partial E}{\partial\Delta\boldsymbol{\mu}_a} = \mathbf{A}\Delta\boldsymbol{\mu}_a - \mathbf{b} = \mathbf{0}, \tag{9}$$

where $\mathbf{g}(\Delta\boldsymbol{\mu}_a) = \mathbf{A}\Delta\boldsymbol{\mu}_a - \mathbf{b}$ is the gradient of E. Three iterative algorithms—projection onto convex sets,[20] conjugate gradient descent,[21,22] and the simultaneous algebraic reconstruction algorithm,[4,23] all based on the perturbation model in Eq. (7)—were used for image reconstruction.

1. Projection onto Convex Sets

POCS is a sequential projection method that reaches the intersection point of L convex constraint sets by the sequential and iterative projection of the current estimate of the solution onto each set C_l (i.e., the set that satisfies the lth constraint), $l = 1, 2, \ldots, L$. A set is convex if any linear combination $tx + (1 - t)y$ of two of its elements x and y, with $0 < t < 1$, also belongs to the set. Some familiar examples of convex sets are circles, lines, and cubes. Letting $\Delta\boldsymbol{\mu}_a^n$ represent the estimate of $\Delta\boldsymbol{\mu}_a$ at the nth iteration, each step in POCS can be represented by

$$\Delta\boldsymbol{\mu}^{n+1} = P_L \circ P_{L-1} \circ \cdots \circ P_1 \Delta\boldsymbol{\mu}^n. \tag{10}$$

Here, the circle operator denotes the conformation of functions, P_l represents the projection operator onto C_l, such that $P_l\Delta\boldsymbol{\mu}_a^n$ is the element in C_l that is closest to $\Delta\boldsymbol{\mu}_a^n$. Each iteration in POCS consists of one use of all L projection operators. Youla[20] used the fixed-point theorem of functional analysis to prove that, as long as the intersection of the constraint sets is not empty and each constraint set is convex, iterative projections onto these sets will converge to their intersection.

The set of solutions to each linear equation in Eq. (7) is a convex set. An advantage of POCS is that it can easily incorporate nonlinear constraints in addition to these linear equations if the sets of solutions satisfying these constraints are convex. The usual source for these nonlinear constraints is *a priori* information, i.e., known properties of the media that help to regularize the reconstruction results. An example of this would be a range constraint, which limits the values of the reconstructed results. See Ref. 20 for other useful constraints and their associated projection operators. When only the linear equations are used, POCS is equivalent to the arithmetic reconstruction technique (ART) proposed by Gordon *et al.*[29] for reconstruction of 3-D structures from 2-D electron micrographs and for x-ray imaging. (This is not to say, however, that the POCS algorithm is strictly valid only for tomographic-imaging modalities, such as x-ray CT, in which the energy traverses the medium along straight-line paths. In contrast to algorithms based on the projection-slice theorem, POCS can be used to solve any system of linear equations, whatever their physical origin.)

2. Simultaneous Algebraic Reconstruction Technique

The SART algorithm, developed by Anderson and Kak[23] in 1984, combines the positive features of ART and the simultaneous iterative reconstruction technique[30] (SIRT). Whereas the projections are applied sequentially in ART, in SIRT the computed changes in all projections are averaged, and the average is used to update the reconstruction. This usually has the effect of suppressing certain types of artifacts that are characteristic of ART reconstructions, but it converges more slowly. SART updates the reconstruction simultaneously, as in SIRT, but with an efficiency equal to or better than that of ART. The formula for computing the nth estimate of the absorption perturbation in the jth voxel is

$$\Delta\mu_{a,j}^n = \Delta\mu_{a,j}^{n-1} + \frac{\displaystyle\sum_{i=1}^{I} w_{ij} \frac{\Delta R_i - \displaystyle\sum_{j'=1}^{J} w_{ij'}\Delta\mu_{a,j'}^{n-1}}{\displaystyle\sum_{j'=1}^{J} w_{ij'}}}{\displaystyle\sum_{i=1}^{I} w_{ij}}. \tag{11}$$

When used in CT imaging, this algorithm can yield reconstructions of good quality and numerical accuracy in only one iteration.[4,23] (When applied to linear systems such as those generated by an ODT measurement, the rate of convergence is lower. However, as was explained above for the POCS algorithm, this does *not* imply SART is really valid only for straight-line tomographic-imaging problems. It is an algebraic method suitable for finding the solution to any system of linear equations.)

3. Conjugate Gradient Descent

CGD, like SART, uses all detector readings simultaneously to compute each update of the estimated absorption perturbation. The formula for computing $\Delta\boldsymbol{\mu}_a^n$ is

$$\Delta\boldsymbol{\mu}_a^n = \Delta\boldsymbol{\mu}_a^{n-1} - \alpha^n \mathbf{d}^n, \tag{12}$$

where

$$\alpha^n = \frac{\|\mathbf{g}^{n-1}\|^2}{\|\mathbf{W}\mathbf{d}^n\|^2},$$

$$\mathbf{d}^n = -\mathbf{g}^{n-1} + \beta^n \mathbf{d}^{n-1},$$

$$\beta^n = \frac{\|\mathbf{g}^{n-1}\|^2}{\|\mathbf{g}^{n-2}\|^2},$$

$$\mathbf{g}^{n-1} = \mathbf{A}\Delta\boldsymbol{\mu}_a^n - \mathbf{b} = \mathbf{g}^{n-2} - \alpha^{n-1}\mathbf{A}\mathbf{d}^{n-1}.$$

$\mathbf{A}$ and $\mathbf{b}$ are as defined previously, $\Delta\boldsymbol{\mu}_a^0$ is an initial estimate of the perturbation, and the initial values taken for the other quantities are $\mathbf{g}^0 = \mathbf{A}\Delta\boldsymbol{\mu}_a^0 - \mathbf{b}$, $\beta^1 = 0$, and $\mathbf{d}^1 = -\mathbf{g}^0$, where $\mathbf{g}^n$ and $\mathbf{d}^n$ are, respectively, the gradient and the conjugate gradient vectors. As a consequence of the coefficient β^n in the formula for $\mathbf{d}^n$, $\{\mathbf{d}^n\}$ is $\mathbf{A}$-orthogonal. That is, the $\mathbf{A}$-weighted inner product $(\mathbf{d}^n)^T\mathbf{A}\mathbf{d}^m = (\mathbf{W}\mathbf{d}^n)^T(\mathbf{W}\mathbf{d}^m)$ equals zero if $n \neq m$. α^n is called the step size. Theoretically, this algorithm should converge after at most J iterations, because $\{\mathbf{d}^1, \mathbf{d}^2, \ldots, \mathbf{d}^J\}$ spans

the solution space. In practice, round-off error may prevent convergence; thus a convergence criterion is needed.

B. Regularization

Strong scattering dilutes the effects of perturbations in the medium and distributes the effect of a localized perturbation among many detectors. Consequently, columns corresponding to adjacent voxels in the weight matrices of Eq. (7) may be nearly identical. The mathematical significance of this is that the linear systems that arise in practice typically are ill conditioned. This is a reflection of the physics of the situation. Multiple scattering is a smoothing process. Very different configurations of absorbers can give quite similar outputs on the surface. Therefore, as was stated above in the subsection on POCS, in practice it is necessary to regularize the computation in order to obtain a physically correct solution.

We examined the effect of ill conditioning and the efficacy of different regularization schemes by applying the reconstruction algorithms with no regularization and again with a positivity constraint on the reconstruction results. This constraint was imposed after each iteration:

$$\Delta\mu_{a,j}^{n} = 0 \text{ if } \Delta\mu_{a,j}^{n} < 0. \tag{13}$$

1. Constrained Conjugate Gradient Descent

The CGD method is the most efficient of the three algorithms but is not able to produce good-quality images because of the difficulty in applying range constraints. The CGD method iteratively updates the reconstruction on the basis of the previous reconstruction $\Delta\boldsymbol{\mu}_a^{n-1}$ and all the preceding gradient vectors $\{\mathbf{g}^0, \mathbf{g}^1, \ldots, \mathbf{g}^{n-1}\}$ and conjugate gradient vectors $\{\mathbf{d}^1, \mathbf{d}^2, \ldots, \mathbf{d}^n\}$. Imposition of positivity constraints on $\Delta\boldsymbol{\mu}_a^{n-1}$ leads to miscalculation of the gradient and the conjugate gradient vectors and results in the loss of the **A**-orthogonality properties. Consequently, the conjugate gradient vectors $\{\mathbf{d}^1, \mathbf{d}^2, \ldots, \mathbf{d}^J\}$ do not span the solution space with this sort of regularization, so the reconstruction will not converge after J iterations. The reconstruction may even diverge in some cases.

In this study a technique to detect divergence when range constraints are imposed on the reconstruction was used. The reconstruction is diverging if the ratio of two consecutive mean-squared errors,

$$r \equiv \frac{E^n}{E^{n-1}} = \frac{E(\Delta\boldsymbol{\mu}_a^n)}{E(\Delta\boldsymbol{\mu}_a^{n-1})},$$

where $E(\Delta\boldsymbol{\mu}_a^n)$ was defined in Eq. (8), is greater than one. It is known that if the mean-squared error increases during any one iteration, it will continue to increase in all subsequent iterations. When divergence is detected, the conjugate-gradient vector is reset, i.e., we take $\mathbf{d}^n = \mathbf{0}$, and the CGD reconstruction is restarted with $\Delta\boldsymbol{\mu}_a^{n-1}$ as the initial estimate of $\Delta\boldsymbol{\mu}_a$. That is, in the worst-case limit, the constrained CGD reduces to a standard gradient-descent algorithm.

2. Weight-Matrix Rescaling

To suppress numerical errors and accelerate convergence, we employed a matrix-rescaling technique. The effect of rescaling the weight matrix is to make it more uniform; this can potentially improve its conditioning.[21] Two rescaling criteria were applied: (1) rescaling the maximum of each column to 1, i.e., $w'_{ij} = w_{ij}/\max_{i=1}^{I}\{w_{ij}\}$; (2) rescaling the average of each column to 1, i.e., $w''_{ij} = w_{ij}/\sum_{i=1}^{I} w_{ij}$. Reconstructions were also computed without any rescaling in order to gauge the efficacy of this technique.

4. Methods

We performed numerical studies to examine the capability of the algorithms (see Section 3) derived from our theoretical considerations (see Section 2) for reconstructing images of the interior properties of dense-scattering media by analyzing measurements made at the surface. In order to reduce the amount of computation, we took full advantage of all symmetry elements present in each problem.

A. Coordinate System

Figure 1 shows cross-sectional and longitudinal views of the phantom geometry used for this study. Cylindrical coordinates (ρ, φ, z) were used, with distances in the ρ and z dimensions measured in multiples of one mean free path length (mfp) and the angle φ measured in degrees. The outer boundary of the phantom volume is $\rho = 10$ mfp, and although the cylinder axis is infinitely long, the forward and the inverse computations are restricted to the portion $|z| \le 20$ mfp. This 3-D volume was discretized into 16,400 voxels bounded by surfaces of constant $\rho = n_\rho/2$ mfp, $n_\rho = 1, 2, \ldots, 20$; of constant $\varphi = \varphi(\rho) = 360n_\varphi/(2n_\rho - 1)$ degrees, $n_\varphi = 0, 1, \ldots, 2(n_\rho - 1)$; and of constant $z = \pm(n_z + 0.5)$ mfp, $n_z = 0, 1, \ldots, 20$. There are 400 voxels in each transectional (ρ, φ) plane. All voxels have the same volume but different shapes, varying from a cylindrical central voxel to progressively more brick-shaped voxels as ρ increases.

B. Monte Carlo Simulations

The numerical studies employed Monte Carlo methods to compute the internal light distributions and the flux of light reemitted across the surface of 3-D cylindrical, isotropically scattering media. In all cases the cylinder axis was infinitely long, its diameter was 20 mfp, and the light source was a pencil beam directed normally to the surface. Each photon incident upon a medium underwent repeated scattering until it either was absorbed in the interior or escaped.

The internal light distribution was calculated for a homogeneous, cylindrical medium; the average collision density was computed in each of 16,400 voxels.

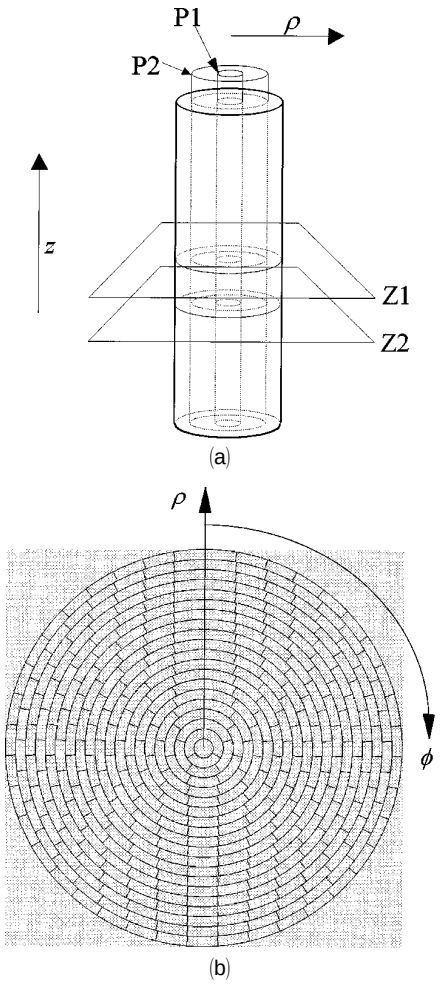

Fig. 1. (a) Longitudinal view of a portion of the cylindrical reference medium with coordinates z and ρ explicitly indicated, illustrating the division of the volume into layers by planes, (Z1 and Z2) perpendicular to the cylinder axis, i.e., by surfaces of constant z, and the division of the layers into rings by a set of surfaces of constant ρ (P1 and P2). (b) A cross-sectional view, showing the voxel geometry and the cylindrical coordinate system used in this study; the z direction is perpendicular to the plane of the sketch.

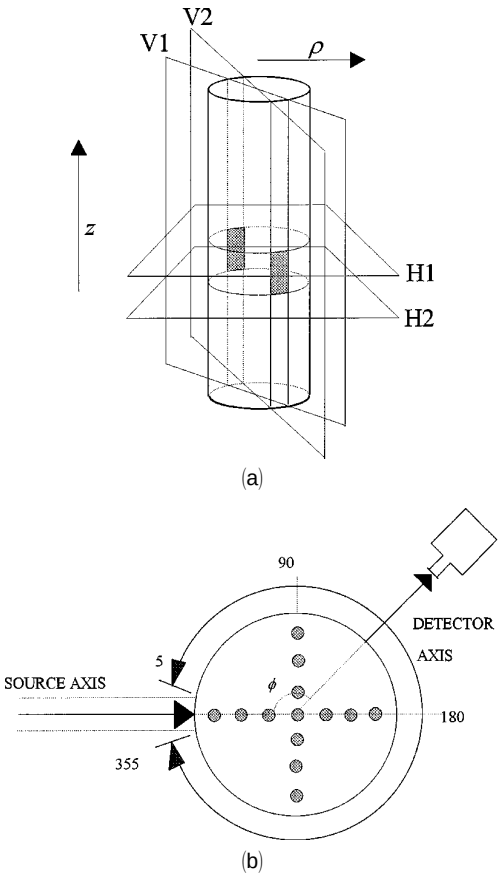

Fig. 2. (a) Longitudinal view of a portion of the cylindrical reference medium with coordinates z and ρ explicitly indicated, illustrating the division of the surface into bands by planes (H1 and H2) perpendicular to the cylinder axis and the bands into sectors by a second set of planes (V1 and V2) intersecting along the axis. (b) Simulation source and detector configurations.

These were arranged in forty-one 1-mfp-thick layers perpendicular to the cylinder axis, with 400 voxels in each layer; each voxel's volume was $\pi/4$ mfp^3 (i.e., $\pi r^2 h/400$); see Fig. 1. The output was reported in units of collisions per unit volume per incident photon. The refractive-index ratio n between the medium and its surroundings was 1.33:1. Photons approaching the boundary were internally reflected according to the reflection probability for unpolarized light. The medium was nonabsorbing. Each history was terminated when the photon escaped from the medium. A total of 2×10^8 photons were launched into the medium, and the number of collisions occurring in each voxel during each 0.5-mfp interval of the total distance propagated through the medium was counted. As the speed of light is constant in a homogeneous medium, this produced a calculation of the time-resolved collision density in each voxel. These results were also used in time- and frequency-domain studies, not reported on here, in addition to the work that is presented. The temporal profiles were subsequently integrated to determine the cw collision density in each voxel.

Detector readings were calculated in separate simulations from those that computed the collision densities; see Fig. 2. The cylinder's surface was first divided into 41 bands by planes perpendicular to its axis with the central band bisected by the plane containing the source. Each band was then divided into 36 congruent areas by lines parallel to the axis. The detectors were cosine detectors at the surface, evenly placed at 10° intervals about the cylinder. Each detector counted all photons emerging from the cylinder within a patch of surface of area $5\pi/9$ mfp^2 (i.e., $2\pi rh/36$). The output was reported in units of exiting photons per unit area per unit solid angle per incident photon. The readings of detectors in only the central band were actually used by the reconstruction algorithms.

A correlated sampling technique was employed to reduce the statistical errors associated with the simulation results. Each photon in the heterogeneous test medium followed exactly the same path as

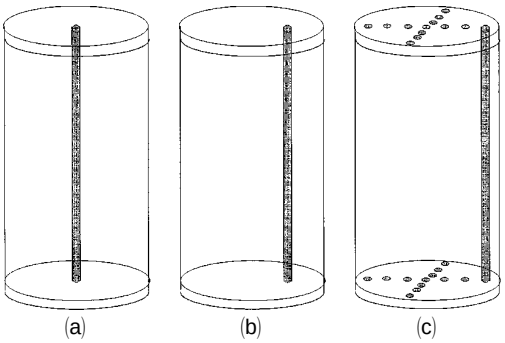

Fig. 3. Phantoms modeled in the Monte Carlo simulations: (a) centered rod, (b) off-axis rod, and (c) 13 rods.

its counterpart in the homogeneous reference medium. If its trajectory intersected a heterogeneity, or black body absorbers in all the examples in this report, then it contributed to a detector response for the reference medium only; if it did not, then it contributed equally to the response of a reference-medium detector and the detector at the same location on the target medium. This minimizes the effect of randomness on the difference between the readings of the paired detectors. In addition, because the responses of both sets of detectors were calculated in a single run, their differences could be calculated simultaneously. This eliminated the need to perform subtractions in a separate postprocessing step, with the attendant possibility of small effects being reported as zero as a consequence of the finite precision of the reported results.

Detector readings were calculated for three distinct test media; see Fig. 3. In the first case [Fig. 3(a)] the heterogeneity was a single 2-mfp-diameter black rod whose axis coincided with the cylinder axis. In the second case [Fig. 3(b)] the heterogeneity was a single 2-mfp-diameter rod whose axis was halfway between the cylinder axis and the boundary, and detector readings were calculated for three different locations of the source. In these cases, $n = 1{:}1$, $\mu_a = 0.0$, and 5×10^7 photons were launched into the medium. That is, there was no internal reflection at the boundaries of these target media, in contrast to the index-mismatched boundary of the medium modeled in the collision-density calculations. In the third case [Fig. 3(c)] the heterogeneity was thirteen 0.5-mfp-diameter rods in a fourfold symmetric cruciform array, and detector readings were calculated for six different locations of the source, with the cylinder rotated through an angle of 9° between successive measurements. In these computations, $n = 1.33{:}1$, $\mu_a = 0.0$, and 2×10^8 photons were launched into the medium. The cw detector responses were calculated by integration of the temporal profiles that were the direct output of the simulations.

The use of black absorbers in these tests violates the linearity assumption in the theoretical and the algorithmic developments. In reality the self-shadowing effect of an absorber produces an essentially hyperbolic dependence of ΔR on $\Delta\mu_a$, and the mutual coupling effect of two absorbers results in a net ΔR that is smaller than the sum of those produced by either of the two acting independently.[31] This is the flux-depression effect well known in reactor physics.[26] However, in assessing the practical utility of an imaging scheme, especially one that requires comparing the responses of a target medium to a reference, it is essential to determine the sensitivity of the algorithm to violations of its underlying premises. The decision to use black absorbers was made as part of an effort to determine the limitations of the imaging methods described in this report. It also conferred two practical benefits that partially offset its disadvantages. First, the use of weaker perturbations would have required the simulation of a larger number of photon histories to produce statistically significant calculations of ΔR. Second, it simplified the computations *vis-à-vis* a finite-absorption model in which the heterogeneity's μ_T is different from that of the background.

All simulation programs were written in standard FORTRAN 77 and were performed on IBM RS6000 workstations of the Center for Advanced Technology in Computer Applications and Software Engineering (CASE Center) at Syracuse University. Because the runs shared time with other jobs on these platforms and because reboots and system maintenance caused many runs to be prematurely terminated, it was not possible to measure the time required for the simulations directly. However, by extrapolating the time required for short test runs, one can reasonably estimate that the average time required for every 10^7 photon histories was between 20 and 25 h in both the collision-density and the detector-reading calculations.

C. Weight-Function Calculation

The intensity ϕ is readily obtained from the Monte Carlo simulation (MCS)-computed collision density, as collision density is simply the product $\mu_T\phi$. As the adjoint can also be computed by solving a forward problem (see Section 2), the same collision density-to-cross section ratio was used for ϕ^+. The (ρ, φ) coordinates of the computed ϕ^+ were rotated through the central angle between source and detector, and the product of ϕ and ϕ^+ was computed in each voxel. To account for the factor of $1/4\pi$ in Eq. (5), image-reconstruction results were multiplied by 4π to produce the final computed $\Delta\boldsymbol{\mu}_a$. The algebraic sign in Eq. (5) is accounted for because in practice we defined ΔR as $R_0 - R$ and $\Delta\boldsymbol{\mu}_a$ as $\boldsymbol{\mu}_a - \boldsymbol{\mu}_a^0$.

D. Image Reconstruction

Image reconstructions were performed with simulated detector readings as input, by all three algorithms, with and without range constraints, and with and without rescaling of the weight matrix.

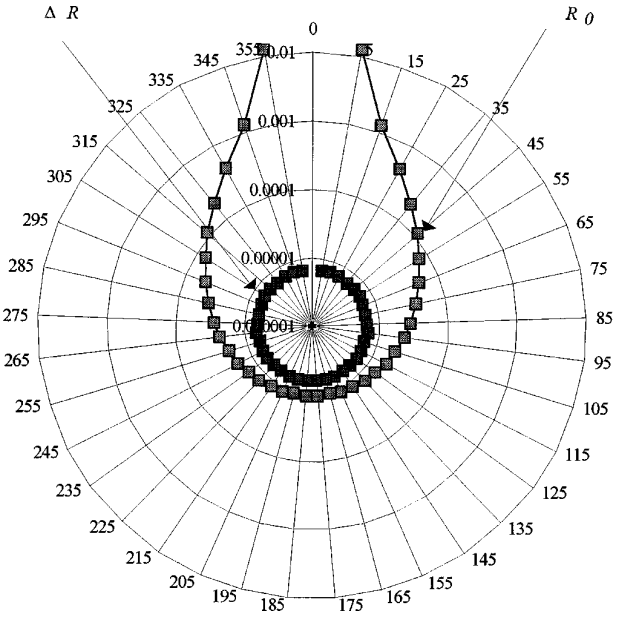

Fig. 4. Monte Carlo simulation results: polar plot of the logarithms of the absolute intensities (R_0) and the intensity differences ($\Delta R = R_0 - R$).

Three types of reconstructions were computed: (1) 3-D reconstruction, in which each voxel was individually considered; (2) 2-D reconstruction, in which *a priori* knowledge of symmetry in the direction parallel to the cylinder axis was assumed; (3) 2-D limited reconstruction, in which it was assumed that only those voxels in the plane of the detectors contribute to the detector readings (i.e., that photons that scatter out of the plane of the source and detectors do not subsequently scatter back in). Convergence rate and image quality were evaluated for each combination of algorithm, rescaling technique, and constraints.

5. Results

A. Simulation Results

Polar logarithmic plots of the computed absolute detected intensities (R_0) and the intensity perturbations (ΔR) caused by the centered absorber are shown in Fig. 4. In this instance the source was incident upon the medium at $\varphi = 0°$, where φ is the angular dimension in the cylindrical polar coordinate system (see Subsection 4.A.). Detectors were positioned at 10° intervals in φ about the phantom. R_0 falls by more than 3 orders of magnitude as φ increases from 0°–10° to 170°–180°, whereas ΔR is nearly constant. In fact, the difference between the greatest and the least values of ΔR is ~7% of the mean value. The same ΔR data are shown in a linear Cartesian plot in Fig. 5(a), along with the quadratic least-squares fit; the correlation coefficient is 0.73. This plot reveals that much of the variation in ΔR among different detectors is attributable to random noise, but there is also a small systematic variation in ΔR with φ (see Section 6). Plots of ΔR versus φ for the case of the off-center absorber with sources located at $\varphi = 0°$, 90°, and 180° and detectors positioned at 10° intervals about the phantoms are shown in Fig. 5(b). ΔR for a source at 270° is the mirror image, about $\varphi = 180°$, of the data for the 90° source. Note that values of φ plotted on the abscissa refer to the *absolute* location of the detector about the cylinder, as shown in the sketch accompanying Fig. 5(b), *not* to the relative angle between source and detector.

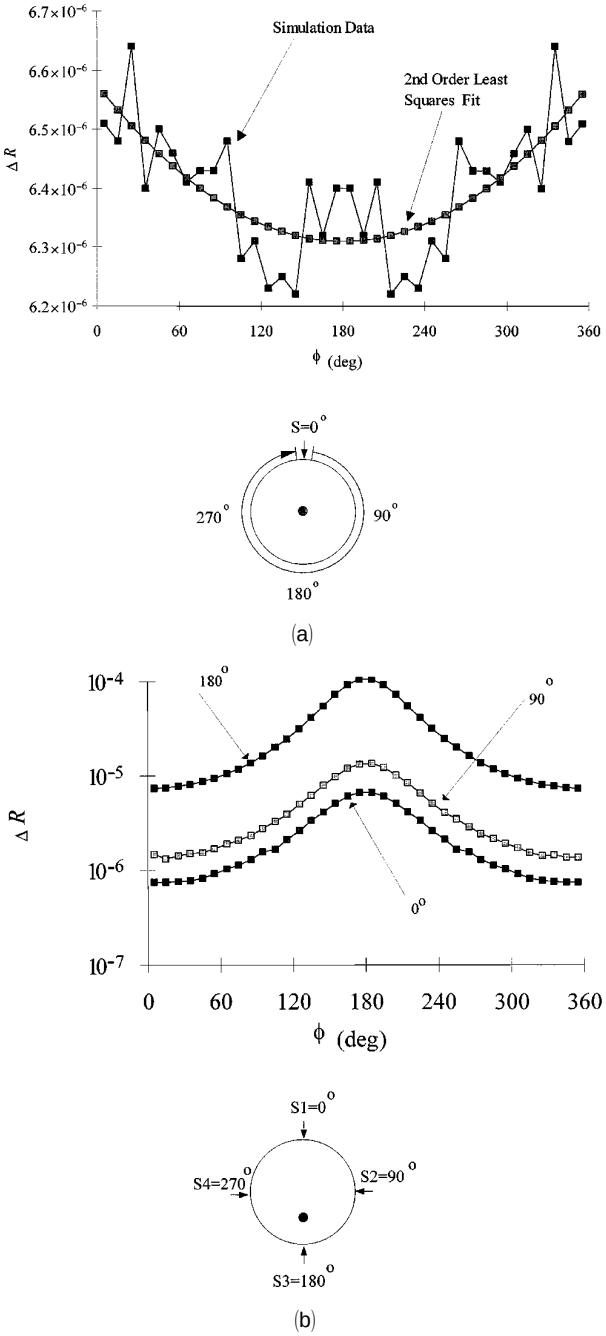

Fig. 5. (a) Monte Carlo simulation results: intensity differences ($\Delta R = R_0 - R$) and their second-order least-squares fit for the centered absorber. The correlation coefficient of the fit is 0.73. (b) Monte Carlo simulation results: intensity differences ($\Delta R = R_0 - R$) for the off-center absorber; the 270° data are the mirror image (with respect to 180°) of the 90° data.

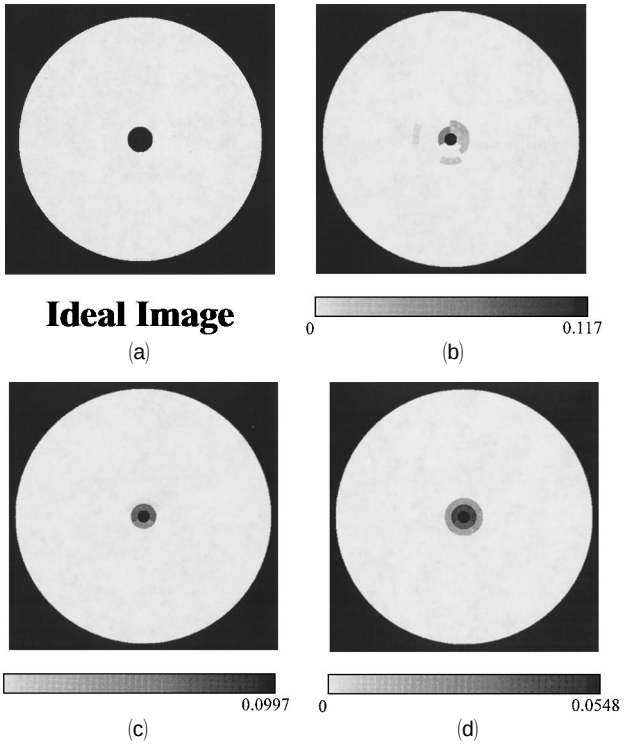

Fig. 6. Two-dimensional reconstructed images of the centered-rod phantom after 10,000 iterations: (a) The target: the white disk represents a cross-sectional cut through the cylinder, and the black area within it indicates the location, the size, and the shape of the heterogeneity ($\Delta\mu_a = \infty$). Reconstructions by the (b) POCS, (c) CGD, and (d) SART algorithms. The maximum value of the reconstructed $\Delta\mu_a$ is explicitly indicated on the linear scale, shading gradually from white to black, under each image.

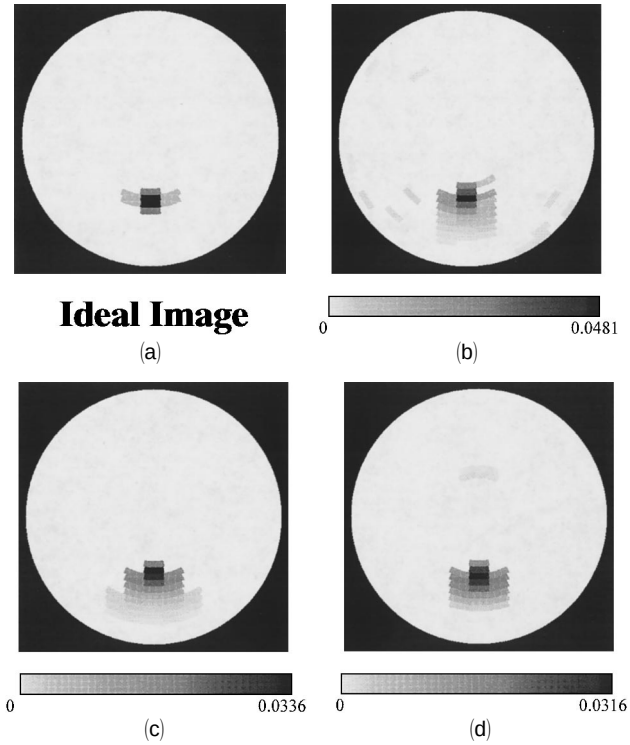

Fig. 7. 2-D reconstruction results of the off-center rod phantom after 10,000 iterations: (a) The target, (b) POCS reconstruction, (c) CGD reconstruction, and (d) SART reconstruction.

B. Reconstruction Results

These results (Figs. 6–12) are displayed as gray-scale images. The first panel in each figure shows the target for the reconstruction; a white disk represents a cross-sectional cut through the cylinder, and the black area within it indicates the location, the size, and the shape of the heterogeneity ($\Delta\mu_a = \infty$). The linear perturbation model must, however, reconstruct a finite value for $\Delta\mu_a$.[31] Under each image is a linear scale shading gradually from white to black with the maximum value of the reconstructed $\Delta\mu_a$ explicitly indicated in each.

Reconstructed images of the centered rod [Fig. 6(a)], the off-center rod [Fig. 7(a)], and the 13-rod [Fig. 8(a)] phantoms, comparing the performance of the POCS, CGD, and SART algorithms, are shown in Figs. 6, 7, and 8, respectively. All these results were obtained from 2-D reconstructions with the rescaled weight matrix $\mathbf{W}'$ (maximum value in each column set equal to 1.0; see Section 3) and a positivity constraint on the results (in addition, because the MCS employed correlated sampling, ΔR is necessarily nonnegative). Instead of using a convergence criterion, we arbitrarily terminated all but one reconstruction after 10,000 iterations. The exception was the SART reconstruction of the 13-rod phantom, which was allowed to proceed for 100,000 iterations.

The results shown in Figs. 9–11 are the 3-D reconstructions corresponding to the same three phantoms. The same constraints and rescaling techniques were used as in the 2-D reconstructions. Because of the larger number of computations performed, the 3-D reconstructions needed more time per iteration, and the reconstructions of the centered-rod and the 13-rod phantoms were terminated after 1000 iterations. However, the reconstructions of the off-center phantom were permitted to proceed for 10,000 iterations.

Two-dimensional limited reconstructions (weights only in the $z = 0$ section of the cylinder are considered) of the off-center rod phantom, with each of the three algorithms, are shown in Fig. 12. The same constraints and rescaling techniques were used as in the 2-D and the 3-D reconstructions.

In all the one-rod cases the internal-reflection properties of the media used for the detector-reading computations were different from what was modeled in the weight-function calculations (see Subsection 4.B.). We used the value $n = 1.00$ when computing the detector readings and the value $n = 1.33$ when calculating the weights. This systematic error did not affect the ability of the reconstruction algorithm to locate and size the heterogeneities accurately (see Section 6).

C. Comparison of Algorithms, Effect of Positivity Constraints, and Effect of Rescaling

Graphs of the mean-squared error E versus the number of iterations for 2-D reconstructions of the

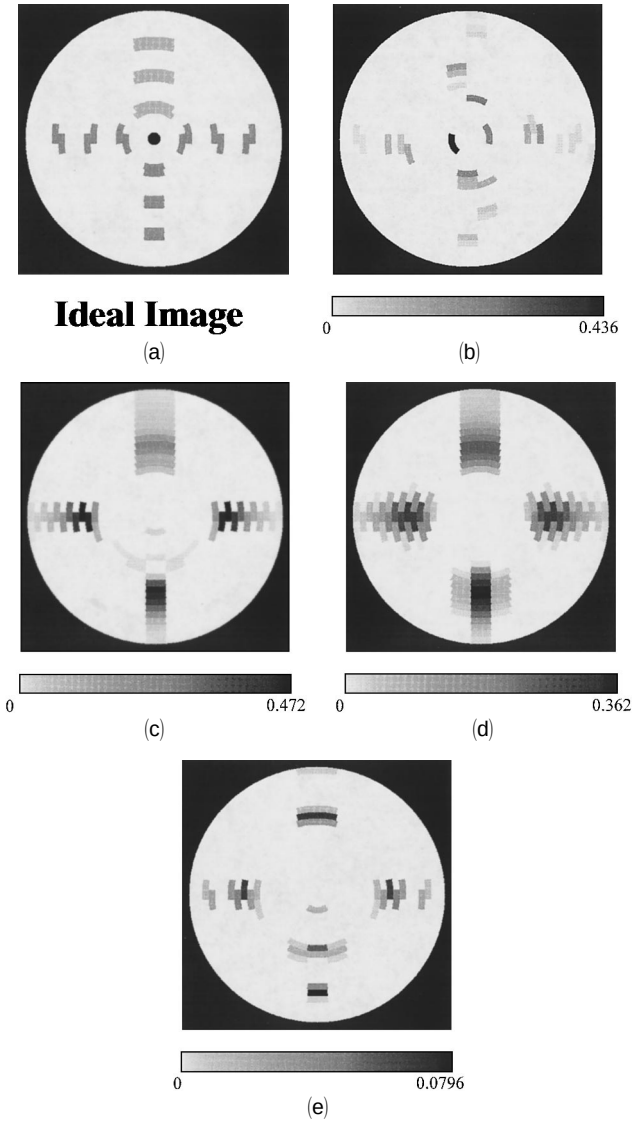

Fig. 8. 2-D reconstructed images of the 13-rod phantom after 10,000 iterations: (a) The target. Reconstructions by the (b) POCS, (c) CGD, (d) SART, (10,000 iterations), and (e) SART (100,000 iterations) algorithms.

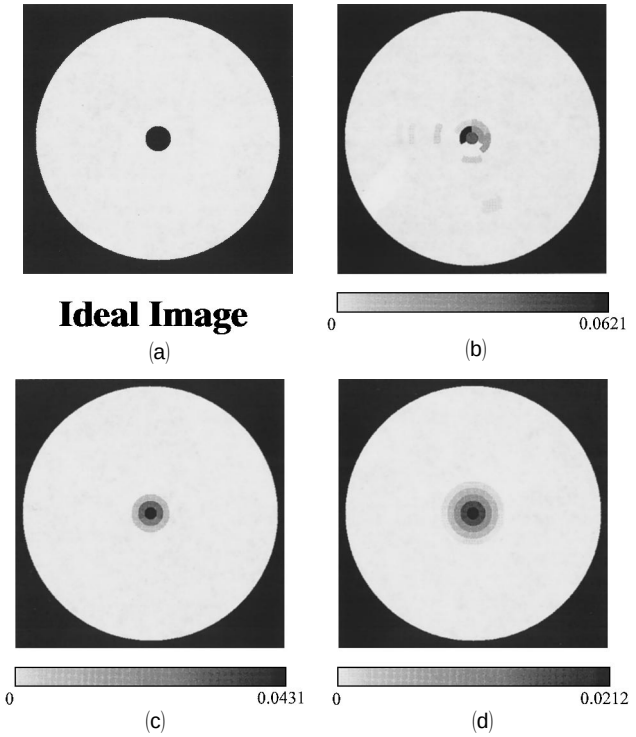

Fig. 9. 3-D reconstructed images of the centered-rod phantom after 1,000 iterations: (a) The target. Reconstructions by the (b) POCS, (c) CGD, and (d) SART algorithms.

off-center rod phantom are shown in Fig. 13. Examination of the curves obtained for the three algorithms when there was no positivity constraint imposed [Fig. 13(a)] shows that the rate of decrease of E was greatest for the CGD algorithm. However, the mathematical solution to which the algorithm converged was physically wrong. The rate of decrease of E associated with the constrained CGD algorithm [Fig. 13(b)] is much lower and is comparable to those seen for the constrained POCS and constrained SART algorithms; however, the accuracy of the reconstructed images is much higher.

The impact of imposing positivity constraints on $\Delta\boldsymbol{\mu}_a^n$ is seen directly in the reconstructed images shown in Fig. 14. The images reconstructed by the CGD algorithm without and with positivity constraints are shown for both the centered rod [Fig. 14(a)] and the off-center rod [Fig. 14(b)] phantoms.

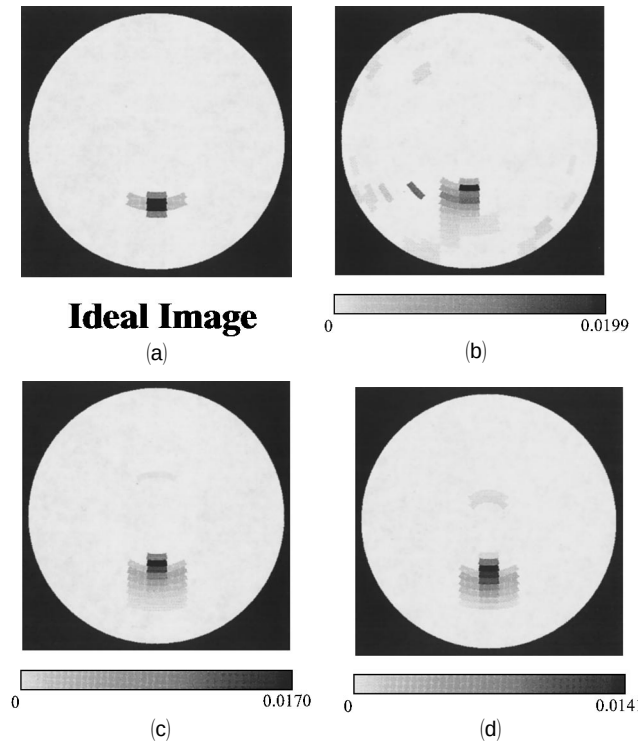

Fig. 10. 3-D reconstruction results of the off-center rod phantom after 10,000 iterations: (a) The target. Reconstructions by the (b) POCS, (c) CGD, and (d) SART algorithms.

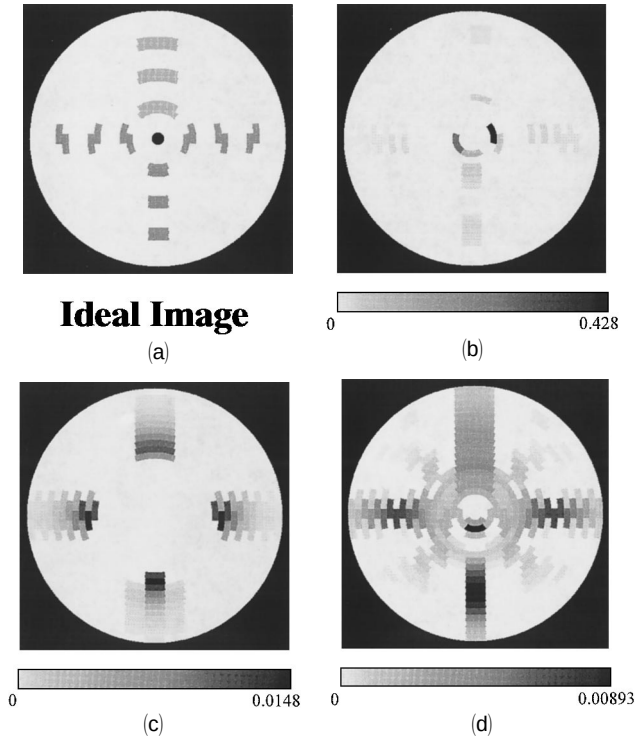

Fig. 11. 3-D reconstructed images of the 13-rod phantom after 1,000 iterations: (a) The target. Reconstructions by the (b) POCS, (c), CGD, and (d) SART algorithms.

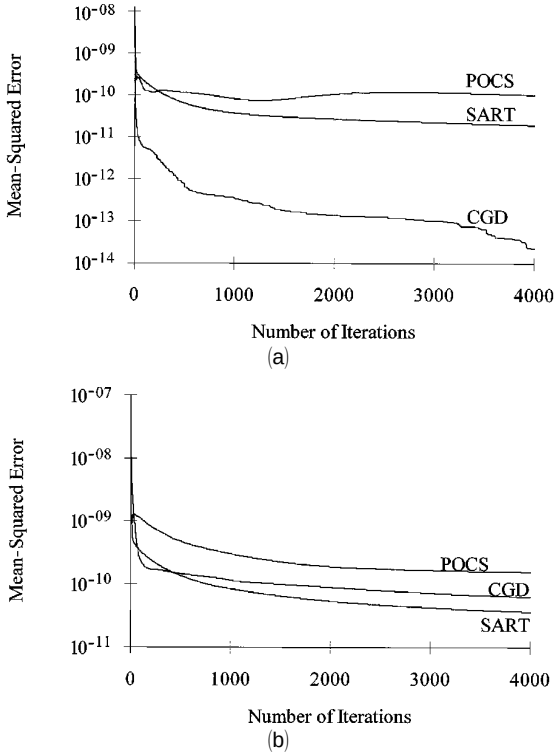

Fig. 13. Mean-squared error versus the number of iterations for different algorithms: (a) unconstrained and (b) constrained reconstructions.

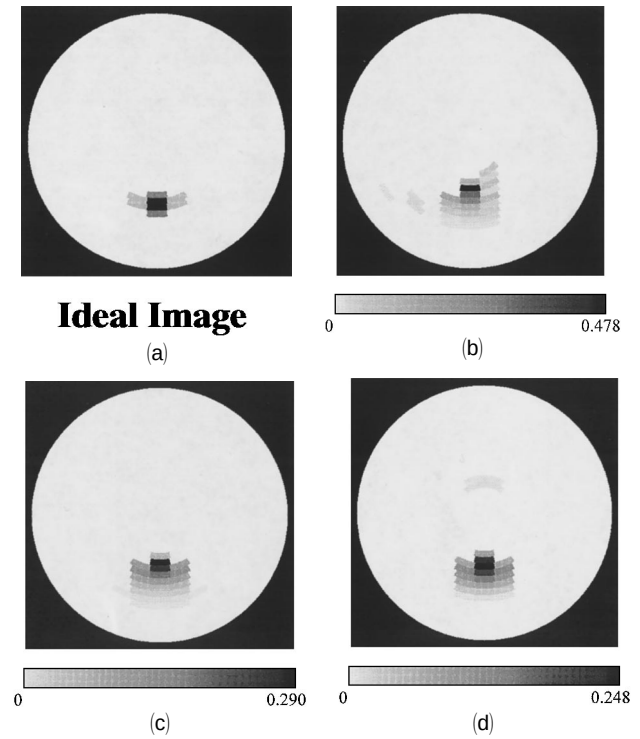

Fig. 12. 2-D reconstruction results of the off-center rod phantom with the weights on only the plane $z = 0$ (i.e., 2-D limited reconstruction) after 10,000 iterations: (a) The target. Reconstructions by the (b) POCS, (c) CGD, and (d) SART algorithms.

The impact of rescaling the weight matrix for each of the three reconstruction algorithms is shown in Figs. 15–17. The images shown are reconstructions of the off-center rod phantom, with positivity constraints on $\Delta\boldsymbol{\mu}_a^n$, as a function of the number of iterations. The results obtained with $\mathbf{W}$, $\mathbf{W}'$, and $\mathbf{W}''$ as the weight matrix are compared for the POCS (Fig. 15), the CGD (Fig. 16), and the SART (Fig. 17) algorithms.

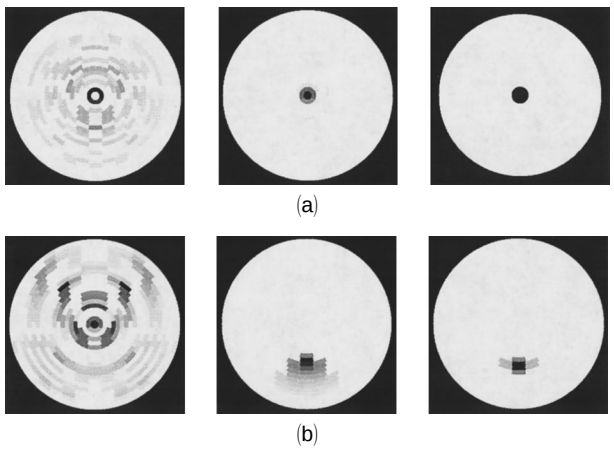

Fig. 14. Image reconstructed without positivity constraints (left), image reconstructed with positivity constraints (center), and target (right) by the CGD algorithm after 10,000 iterations: (a) centered and (b) off-center rod phantom.

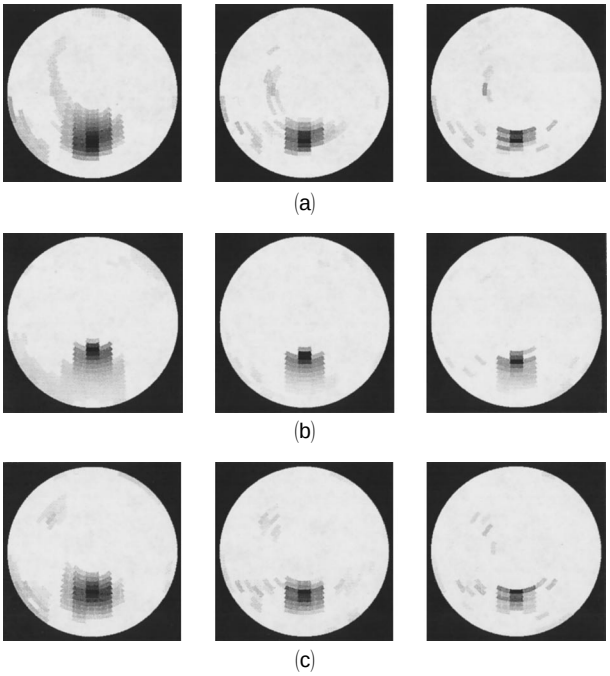

Fig. 15. Reconstructed images obtained by the POCS algorithm and (a) no rescaling (**W**), (b) rescaling the maximum of each column to 1 (**W**′), or (c) rescaling the average of each column to 1 (**W**″). Results are plotted after 100 (left), 1000 (center), and 10,000 (right) iterations.

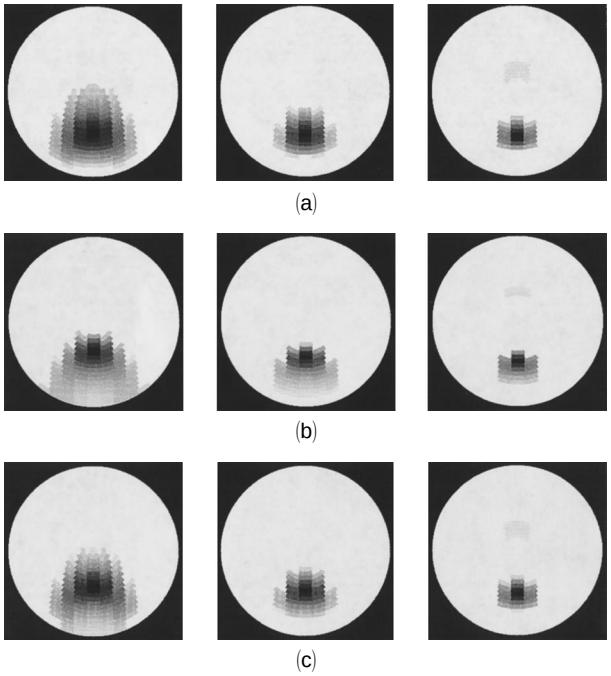

Fig. 17. Same as Fig. 15 except that the reconstructed images are obtained by the SART algorithm.

6. Discussion and Conclusions

The purpose of this study was to derive a useful strategy for imaging highly scattering media with a perturbation model based on transport theory. The perturbation model adopts a first-order approximation to the change in photon intensity, ΔR, caused by the perturbation of the collision cross sections, $\Delta\mu_s$ and $\Delta\mu_a$. It greatly simplifies the inverse problem by introducing a linear imaging operator, the weight matrix **W**, which can be relatively easily inverted by iterative methods. The quality of the image obtained by solving the inverse problem therefore is a function of the accuracy of this model and the forward calculation of the weight matrix.

The computations performed for this study assumed isotropic scattering. The rationale is threefold:

(1) The computations are simpler. The emphasis here was on imaging, i.e., on solving the inverse problem, and the details of the scattering are not important in studying this question.

(2) The correct differential cross sections are not known, and they undoubtedly differ from tissue to tissue. Any differential cross section used would be arbitrary.

(3) Along with all investigations by diffusion theory, we fall back on the transport approximation. In this approximation, μ_T is replaced by the transport cross section, μ_{tr}, defined by

$$\mu_{tr} = (1 - g)\mu_s + \mu_a,$$

where g is the average value of the cosine of the scattering angle. It can be shown[32] that, for a particle going in a given direction, $\lambda_{tr} = 1/\mu_{tr}$ is the average distance it travels in this direction before its direction is randomized. In effect, it is the distance along its original direction to an isotropic collision. For weakly anisotropic scattering it is known that this is a good approximation, and even for the

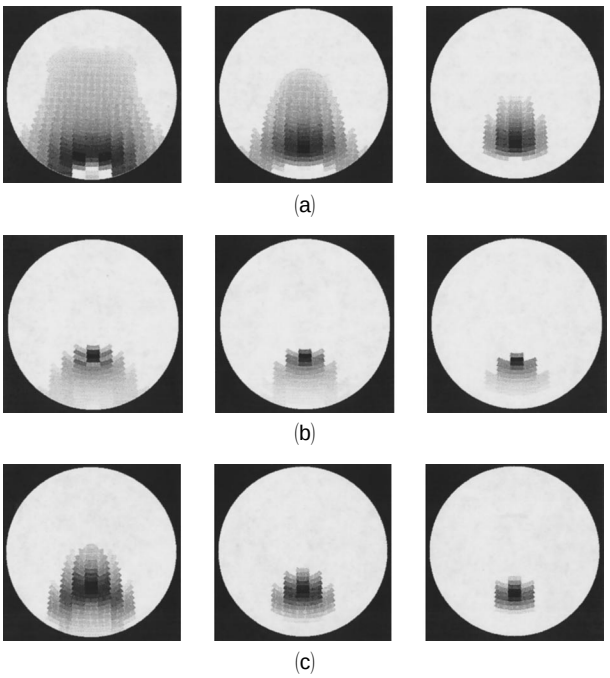

Fig. 16. Same as Fig. 15 except that the reconstructed images are obtained by the CGD algorithm.

strongly anisotropic scattering in tissue it is assumed to be not too bad. It is also a necessary approximation for diffusion calculations to be applicable.

Reconstructed images by diffusion theory along with a perturbation algorithm analogous to our Eq. (6) have been reported by several groups.[33–39] If the voxel dimensions are larger than the diffusion coefficient $D(\mathbf{r})$—and preferably several times that—and the boundary conditions are properly chosen, the performance of a diffusion-based imaging operator can be qualitatively very similar to that of the transport-based operator. Unfortunately, there is as yet no set of standardized problems on which all groups work, so no detailed quantitative comparison of different approaches to either the forward or the inverse problem is possible. In any case, *a priori* knowledge of the medium is required for accurate forward modeling and solving the inverse problem.

It can be seen from Fig. 4 that R_0 falls by more than 3 orders of magnitude as the source–detector angle φ increases from 0° to 180°, whereas ΔR for the case of the centered-rod phantom is nearly constant. This is an encouraging result, as it was predicted on the basis of the perturbation model, according to which the weight at a point on the cylinder axis is independent of φ. The weak dependence of ΔR on φ is remarkable also because the rod, owing to both its volume and its absorption cross section, strongly violates the linearity assumption that underlies the model. As shown in Fig. 5(a), however, ΔR is not absolutely constant in φ. As a consequence of the rod's relatively large (1-mfp) radius, there is some variation in weight across the area it occupies, and the total weight integrated over this area is greatest at $\varphi = 0°$, lowest at $\varphi = 180°$. Therefore ΔR would be expected to fall somewhat as φ increases from 0° to 180°. Consistent with this prediction, the quadratic-curve fit to the data has a minimum at $\varphi = 180°$.

All three curves of ΔR versus φ for the off-center rod in Fig. 5(b) have a maximum at $\varphi = 175°$ or $\varphi = 185°$. The location of the maximum and the fact that ΔR is larger for the $\varphi = 180°$ source than for the $\varphi = 0°$ source are consequences of the absorber location, as shown in the accompanying sketch. The ΔR computed for the case of source $\varphi = 0°$ and detector $\varphi = 175°$ is nearly the same as that for the case of source $\varphi = 180°$ and detector $\varphi = 5°$. This could be interpreted as a direct confirmation of the reciprocity theorem[28] if the (one-point, monodirectional) source and the (finite-area, cosine) detector configurations were interchanged along with their locations. As it is, the small difference between the two computed values for ΔR suggests that the theorem can be used as a check on the outcome of appropriately paired measurements even if the source–detector configurations are not truly reciprocal.

Inspection of Fig. 6 reveals that the CGD algorithm produced a nearly perfect reconstruction of the positions of the rods. Images almost as good were also obtained with the SART and POCS algorithms. For the off-center case, as seen in Fig. 7, all three methods accurately located the absorber with minimal artifacts. Although in all cases the images of the 13-rod phantom, as shown in Fig. 8, were poorer than those obtained for the single-rod phantoms, identification of the general structure of the medium is unmistakable. We believe the inability to resolve the central features of the medium accurately is caused by significant overestimation of the weight in this region, which in turn is caused by the presence of the peripheral absorbing rods (i.e., flux depression). This phantom violates the linearity assumption underlying Eq. (7) the most strongly of all those considered in these studies; the accuracy of the reconstruction would presumably be improved by use of the images shown in Fig. 8 as a modified estimate of the reference medium.

The inverse scattering problem is intrinsically 3-D because of the significant contribution to detector response from photons that propagate out of the source–detector plane and subsequently scatter back to a detector. Thus, unlike CT or magnetic resonance imaging, in which most detected signals arise from slices selected by either the source–detector pairs or by the gradient fields, voxels outside the plane selected by source–detector pairs also should be considered in ODT. The importance of these voxels' contributions depends on the absorption and the scattering cross sections and on the dimensions of the medium. In this study, results from 2-D, 3-D, and 2-D–limited reconstructions were obtained and compared. The 3-D reconstruction results (Figs. 9–11) are similar to those of the 2-D case. This suggests that, although the 3-D reconstruction is most accurate, a 2-D reconstruction, which we make either by assuming the phantom is symmetrical along the z axis (Figs. 6–8) or by using only the weights of voxels in the source–detector plane (Fig. 12), provides reasonably good results while giving the solution in a much shorter computation time—as little as 10% of the time needed for 3-D reconstruction in the study. This may prove to be a useful strategy for obtaining an initial estimate of $\Delta\mu_s$ and $\Delta\mu_a$ in more complex target media. However, the phantoms used in this study have axial symmetry. It is evident that in complex media such as tissue the assumption of axial symmetry typically will be violated. Two-dimensional reconstructions may not provide good results in these cases; additional studies on this topic are needed. For all the phantoms, the comparative trend in image quality of the three algorithms was CGD > SART > POCS. Overall, the reconstructions clearly show that analysis of time-independent data by a perturbation model is capable of resolving the internal structure of a dense-scattering medium.

Two factors, efficiency and quality, are key when choosing a reconstruction algorithm for the inverse scattering problem. High efficiency, defined as the

rate of decrease of the mean-squared error, does not generally guarantee a physically accurate image, as a consequence of modeling error, noise, and accumulation of numerical errors. Some nonlinear constraints derived from *a priori* information may produce better results. The use of constraints, however, reduces the rate of convergence, as shown in Fig. 13. When constrained, all three algorithms converge at approximately the same rate, which is lower than that of their unconstrained counterparts. CGD converges much faster than the other methods when there are no constraints, whereas inspection of Fig. 14 shows that unconstrained CGD provides the worst results. As shown in this figure, the use of constraints proved to be crucial. For both the centered rod and the off-center rod phantoms the reconstruction results when there were no constraints bore no resemblance to the target, and the imposition of constraints resulted in reconstruction of nearly perfect images.

The images presented here also begin to address questions about the sensitivity of the reconstruction algorithms to both random and systematic errors in the data. The MCS yields numerical solutions to the transport equation containing (sometimes significant levels of) noise. Therefore there necessarily was random error in both the computed weight functions and detector readings. There also were three notable sources of modeling error in these data. First, the heterogeneities were blackbody absorbers, which have infinite μ_a. Consequently it is not possible in the present report to compare the MCS detector readings to those computed from Eq. (7), which clearly cannot have infinite solutions. Second, ΔR was computed for cosine detectors that received photons over a finite area, whereas $\mathbf{W}$ was computed for normally directed, single-point, collimated detectors. Third, the index-matched boundary modeled for the one-rod computations differed from the index-mismatched boundary of the collision-density computations. These discrepancies serve as tests of the power of the reconstruction algorithms.

The rescaling techniques improve the reconstruction, especially in the early iterations. Comparison of the results of all three methods, as seen in Figs. 15–17, shows that the reconstructed image with rescaling is very different after 100 iterations from the corresponding result obtained without rescaling. The effect is largest, and most clearly beneficial, when the CGD algorithm is used. A qualitatively similar, but smaller, effect is seen in the results produced by the SART algorithm. Setting the maximum of each column to 1.0 generally produces the best results, followed by setting the average of each column to 1.0, which in turn is better than the result obtained with no rescaling. Although rescaling causes a change in the results produced by the POCS algorithm, it is not clear that there is any improvement in the rate of convergence. When the reconstructions were permitted to proceed for 10,000 iterations, there was much less difference between the images produced by the different weight-matrix varieties. That is, rescaling does not appear to introduce any systematic error into the computation, and it can have the important benefit of increasing the initial convergence rate. As a consequence, an accurate image may be obtained in a smaller number of iterations if these techniques are adopted.

This idea for the matrix-rescaling method was derived from a recognition that, in dense-scattering media, the range of possible weight values corresponding to a particular voxel is strongly dependent on the depth at which it lies in the medium. This results in large variations in the maximum values among the column vectors, $\mathbf{w}_j$, of Eq. (7). Physically, $\mathbf{w}_j$ is an expression of the importance of a particular voxel to the detector response. Voxels having weight-matrix elements with large absolute values will have a greater impact on a detector than voxels with smaller elements. Now it is expected that the CGD method will preferentially update those voxels having the greatest weights; this follows because column vectors that have the largest sum of absolute weights will most strongly influence the computed conjugate gradient. From previous studies we have determined that the largest values of weight typically occur in the vicinity of the sources and the detectors.[15] As these are located near the surface, in early iterations the resultant image will be predominantly localized in these voxels, as shown in Fig. 16(a). The effect of rescaling is to mathematically minimize differences in importance between the weight vectors, leading to a more uniform update of the reconstructed image.

Results shown in Fig. 16(b) demonstrate that, with rescaling, a more accurate reconstruction is achieved with the CGD algorithm after only 100 iterations. Figure 16(c) shows that an improved result is also obtained when the average value of the column vector is set equal to one, but this result would appear inferior to the case when the maximum value is scaled to one [Fig. 16(b)]. The corresponding results for the SART algorithm, which is also a simultaneous method, reveal (Fig. 17) that rescaling produces some improvement in image quality in early iterations, but the magnitude of this effect is less than that observed for CGD. Without rescaling, the SART result is more accurate at early iterations than that obtained by CGD. Inspection of the SART algorithm shows that during the backprojection step, projections to each voxel are divided by the sum of the elements of the column vector for that voxel. This is equivalent to rescaling the average value of each column vector to one. The effect of rescaling on reconstructions obtained with POCS (Fig. 15) is less significant than that on the other algorithms. In POCS the angles between the constraint sets are critical determinants of the convergence rate. We believed *a priori* that rescaling might have the effect of increasing these angles and thereby increase the convergence rate. This effect was not seen in these

results. Mathematical analyses of POCS[20] have shown that the quality of the image finally obtained and the convergence rate may depend strongly on the precise sequence in which the evolving estimate of the solution is projected onto the constraints in Eq. (10). The problem of optimizing the order in which sequential algorithms consider the detector readings needs to be addressed in future studies.

In conclusion, we have demonstrated the successful recovery of patterns of absorption cross-section inhomogeneity embedded in thick, dense-scattering media. The images are accurate for a simple heterogeneity and are substantially correct even in the case of a complex absorption pattern that strongly violates the premises of the physical model underlying the reconstruction algorithms. This study used only cw sources. It is reasonable to suppose that the use of more sophisticated illumination–detection techniques, e.g., time-harmonic[40,41] and time-resolved[42,43] measurements, will provide additional information about a target medium, which could in turn permit reconstruction of more accurate images. Although the quality of some of the results we obtained might seem to imply the sufficiency of cw measurement alone, the optical thickness (20 mfp) studied here *is* sufficiently great that unscattered and singly scattered light are negligible components of the total detector response, *but* these media are nevertheless thinner than many clinically interesting targets. These issues of alternative measurement schemes and optically thicker targets are among those we will take up in the course of future work.

This study was supported in part by National Institutes of Health grant R01 CA59955, by Office of Naval Research grant 00149510063, and by the New York State Science and Technology Foundation.

References

1. H. E. Johns and J. R. Cunningham, *The Physics of Radiology,* 4th ed. (Thomas, Springfield, Ill., 1983).
2. D. D. Stark and W. G. Bradley, Jr., eds., *Magnetic Resonance Imaging,* 2nd ed. (Mosby, St. Louis, Mo., 1992).
3. G. T. Herman, *Image Reconstruction from Projections: The Fundamentals of Computerized Tomography* (Academic, New York, 1980).
4. A. V. Kak and M. Slaney, *Principles of Computerized Tomographic Imaging* (Institute of Electrical and Electronics Engineering, New York, 1988).
5. H. Stark, ed., *Image Recovery: Theory and Application* (Academic, New York, 1987).
6. W. A. Kalender, "X-ray computed tomography—state of the art," in *Medical Optical Tomography: Functional Imaging and Monitoring,* G. J. Mueller, B. Chance, R. R. Alfano, S. R. Arridge, J. Beuthan, E. Gratton, M. Kaschke, B. R. Masters, S. Svanberg, and P. van der Zee, eds., Vol. I511 of SPIE Institute Series (Society of Photo-Optical Instrumentation Engineers, Bellingham, Wash., 1993), pp. 10–27.
7. G. J. Mueller, B. Chance, R. R. Alfano, S. R. Arridge, J. Beuthan, E. Gratton, M. Kaschke, B. R. Masters, S. Svanberg, and P. van der Zee, eds., *Medical Optical Tomography: Functional Imaging and Monitoring,* Vol. I511 of SPIE Institute Series (Society of Photo-Optical Instrumentation Engineers, Bellingham, Wash., 1993).
8. R. R. Alfano, ed., *Advances in Optical Imaging and Photon Migration,* Vol. 21 of OSA Proceedings Series (Optical Society of America, Washington, D.C., 1994).
9. B. Chance and R. R. Alfano, eds., *Optical Tomography, Photon Migration, and Spectroscopy of Tissue and Model Media: Theory, Human Studies, and Instrumentation,* Proc. SPIE **2389,** (1995).
10. O. W. van Assendelft, *Spectrophotometry of Haemoglobin Derivatives* (Thomas, Springfield, Ill., 1970).
11. B. Beauvoit, T. Kitai, and B. Chance, "Contribution of the mitochondrial compartment to the optical properties of the rat liver: a theoretical and practical approach," Biophys. J. 2501–2510 (1994).
12. Y. Wang, J. Chang, R. Aronson, R. L. Barbour, and H. L. Graber, "Imaging scattering media by diffusion tomography: an iterative perturbation approach," in *Physiological Monitoring and Early Detection Diagnostic Methods,* T. S. Mang, ed., Proc. SPIE **1641,** 58–71 (1992).
13. J. Chang, Y. Wang, R. Aronson, H. L. Graber, and R. L. Barbour, "A layer stripping approach for recovery of scattering medium using time-resolved data," in *Inverse Problems in Scattering and Imaging,* M. A. Fiddy, ed., Proc. SPIE **1767,** 384–395 (1992).
14. J. Chang, Y. Wang, R. Aronson, H. L. Graber, and R. L. Barbour, "Time-resolved imaging in dense scattering media," in *Physiological Imaging, Spectroscopy, and Early Detection Diagnostic Methods,* R. L. Barbour and M. J. Carvlin, eds., Proc. SPIE **1887,** 108–119 (1993).
15. H. L. Graber, J. Chang, J. Lubowsky, R. Aronson, and R. L. Barbour, "Near infrared absorption imaging of dense scattering media by steady-state diffusion tomography," in *Photon Migration and Imaging in Random Media and Tissues,* R. R. Alfano and B. Chance, eds., Proc. SPIE **1888,** 372–386 (1993).
16. J. Chang, H. L. Graber, and R. L. Barbour, "Image reconstruction of targets in random media from continuous wave laser measurements and simulated data," in *Advances in Optical Imaging and Photon Migration,* R. R. Alfano, ed., Vol. 21 of OSA Proceedings Series (Optical Society of America, Washington, D.C., 1994), pp. 193–201.
17. W. Zhu, Y. Wang, H. L. Graber, R. L. Barbour, and J. Chang, "A regularized progressive expansion algorithm for recovery of scattering media from time-resolved data," in *Advances in Optical Imaging and Photon Migration,* R. R. Alfano, ed., Vol. 21 of OSA Proceedings Series (Optical Society of America, Washington, D.C., 1994), pp. 193–201.
18. J. Chang, R. Aronson, H. L. Graber, and R. L. Barbour, "Imaging diffusive media using time-independent and time-harmonic sources: dependence of image quality on imaging algorithms, target volume, weight matrix, and view angles," in *Optical Tomography, Photon Migration, and Spectroscopy of Tissue and Model Media: Theory, Human Studies, and Instrumentation,* B. Chance and R. R. Alfano, eds., Proc. SPIE **2389,** 448–464 (1995).
19. W. Z. Zhu, Y. Wang, J. Chang, H. L. Graber, and R. L. Barbour, "Image reconstruction in scattering media from time-independent data: a total least squares approach," in *Optical Tomography, Photon Migration, and Spectroscopy of Tissue and Model Media: Theory, Human Studies, and Instrumentation,* B. Chance and R. R. Alfano, eds., Proc. SPIE **2389,** 420–430 (1995).
20. D. C. Youla, "Mathematical theory of image reconstruction by the method of convex projections," in *Image Recovery: Theory and Application,* H. Stark, ed. (Academic, New York, 1987).
21. P. E. Gill, W. Murray, and M. H. Wright, *Practical Optimization* (Academic, New York, 1981).

22. G. Strang, *Introduction to Applied Mathematics* (Wellesley-Cambridge Press, Wellesley, Mass., 1986).
23. A. H. Anderson and A. C. Kak, "Simultaneous algebraic reconstruction technique (SART): a superior implementation of the ART algorithm," Ultrason. Imag. **6,** 81–94 (1984).
24. G. A. Deschamps and H. S. Garayan, "Antenna synthesis and solution of inverse problems by regularization methods," IEEE Trans. Antennas Propag. **AP-20,** 268–274 (1972).
25. A. Ishimaru, *Wave Propagation and Scattering in Random Media* (Academic, New York, 1978).
26. K. M. Case and P. F. Zweifel, *Linear Transport Theory* (Addison-Wesley, Reading, Mass., 1967).
27. J. Chang, H. L. Graber, and R. L. Barbour, "Progress toward optical mammography: imaging in dense scattering media using time-independent optical sources," in *Proceedings of 1994 IEEE Medical Imaging Conference* (Institute of Electrical and Electronics Engineers, New York, 1995), pp. 1484–1488.
28. H. C. van de Hulst, *Multiple Light Scattering* (Academic, New York, 1980), Chap. 3.
29. R. Gordon, R. Bender, and G. T. Herman, "Algebraic reconstruction techniques (ART) for three-dimensional electron microscopy and x-ray photography," J. Theor. Biol. **29,** 471–481 (1970).
30. P. Gilbert, "Iterative methods for the three-dimensional reconstruction of an object from projections," J. Theor. Biol. **36,** 105–117 (1972).
31. H. L. Graber, R. L. Barbour, J. Chang, and R. Aronson, "Identification of the functional form of nonlinear effects of localized finite absorption in a diffusing medium," in *Optical Tomography, Photon Migration, and Spectroscopy of Tissue and Model Media: Theory, Human Studies, and Instrumentation,* B. Chance and R. R. Alfano, eds., Proc. SPIE **2389,** 669–681 (1995).
32. J. Lamarsh, *Introduction to Nuclear Reactor Theory* (Addison-Wesley, Reading, Mass., 1966).
33. M. Schweiger, S. R. Arridge, and D. T. Delpy, "Application of the finite-element method for the forward and inverse models in optical tomography," J. Math. Imag. Vis. **3,** 263–283 (1993).
34. S. R. Arridge and M. Schweiger, "Sensitivity to prior knowledge in optical tomographic reconstruction," in *Optical Tomography, Photon Migration, and Spectroscopy of Tissue and Model Media: Theory, Human Studies, and Instrumentation,* B. Chance and R. R. Alfano, eds., Proc. SPIE **2389,** 378–388 (1995).
35. S. Feng and F.-A. Zeng, "Perturbation theory of photon migration in the presence of a single defect," in *Advances in Optical Imaging and Photon Migration,* R. R. Alfano, ed., Vol. 21 of OSA Proceedings Series (Optical Society of America, Washington, D.C., 1994), pp. 217–228.
36. K. D. Paulsen and H. Jiang, "Spatially varying optical property reconstruction using a finite element diffusion equation approximation," Med. Phys. **22,** 691–701 (1995).
37. M. A. O'Leary, D. A. Boas, B. Chance, and A. G. Yodh, "Simultaneous scattering and absorption images of heterogeneous media using diffusive wave within the Rytov approximation," in *Optical Tomography, Photon Migration, and Spectroscopy of Tissue and Model Media: Theory, Human Studies, and Instrumentation,* B. Chance and R. R. Alfano, eds., Proc. SPIE **2389,** 320–327 (1995).
38. M. R. Ostermeyer and S. L. Jacques, "Perturbation theory for optical diffusion theory: a general approach for absorbing and scattering objects in tissue," in *Optical Tomography, Photon Migration, and Spectroscopy of Tissue and Model Media: Theory, Human Studies, and Instrumentation,* B. Chance and R. R. Alfano, eds., Proc. SPIE **2389,** 98–102 (1995).
39. R. Model, R. Hünlich, M. Orlt, and M. Walzel, "Image reconstruction for random media by diffusion tomography," in *Optical Tomography, Photon Migration, and Spectroscopy of Tissue and Model Media: Theory, Human Studies, and Instrumentation,* B. Chance and R. R. Alfano, eds., Proc. SPIE **2389,** 400–410 (1995).
40. M. S. Patterson, B. W. Pougue, and B. C. Wilson, "Computer simulation and experimental studies of optical imaging with photon density waves," in *Medical Optical Tomography: Functional Imaging and Monitoring,* G. J. Mueller, B. Chance, R. R. Alfano, S. R. Arridge, J. Beuthan, E. Gratton, M. Kaschke, B. R. Masters, S. Svanberg, and P. van der Zee, eds., Vol. IS11 of SPIE Institute Series (Society of Photo-Optical Instrumentation Engineers, Bellingham, Wash., 1993), pp. 513–533.
41. A. Yodh and B. Chance, "Spectroscopy and imaging with diffusing light," Phys. Today **48**(3), 34–40 (1995).
42. F. Liu, K. M. Yoo, and R. R. Alfano, "Ultrafast laser-pulse transmission and imaging through biological tissues," Appl. Opt. **32,** 554–558 (1993).
43. R. Berg, S. Andersson-Engels, and S. Svanberg, "Time-resolved transillumination imaging," in *Medical Optical Tomography: Functional Imaging and Monitoring,* G. J. Mueller, B. Chance, R. R. Alfano, S. R. Arridge, J. Beuthan, E. Gratton, M. Kaschke, B. R. Masters, S. Svanberg, and P. van der Zee, eds., Vol. IS11 of SPIE Institute Series (Society of Photo-Optical Instrumentation Engineers, Bellingham, Wash., 1993), pp. 397–424.